Simultaneous observation of speed dependence and Dicke narrowing for self-perturbed P-branch lines of O_2 B band

Katarzyna Bielska [a,*], Jolanta Domysławska [a], Szymon Wójtewicz [a], Aleksandr Balashov [a,b],
Michał Słowiński [a], Mariusz Piwiński [a], Agata Cygan [a], Roman Ciuryło [a], Daniel Lisak [a]

[a] Institute of Physics, Faculty of Physics, Astronomy and Informatics, Nicolaus Copernicus University in Toruń, Grudziadzka 5, 87–100 Torun, Poland
[b] Institute of Applied Physics of the Russian Academy of Sciences, Ulyanov str. 46, 603950 Nizhny Novgorod, Russia

ARTICLE INFO

ABSTRACT

We present new measurements of the oxygen B-band transitions in the P branch performed with the cavity ring-down spectroscopy (CRDS) and the cavity mode-width spectroscopy (CMWS) techniques. Systematic deviations on the line intensities observed comparing to our previously published data are explained. We reached agreement on unperturbed line positions at the 40 kHz level and on the line intensities below 0.2% for measurements performed with the above two techniques. With significantly increased spectra signal-to-noise ratio we simultaneously observe the speed dependence of collisional broadening and shifting as well as Dicke narrowing in the pressure range as low as 1.1 kPa.

1. Introduction

Oxygen B band centered around 690 nm and arising from $b^1\Sigma_g^+ (\upsilon = 1) \leftarrow X^3\Sigma_g^- (\upsilon = 0)$ transitions is the second most intense band in the red part of absorption spectrum of the O_2 molecule. Although it is approximately 15 times weaker than the most intense A band, its several applications in the remote sensing of the Earth's atmosphere have been proposed. If used together with the A band, it can lead for instance to reduced uncertainties in the pressure and temperature profiles determined across the atmosphere [1]. The B band contributes to improved parameters of clouds such as their top height and top pressures [2–5] as well as aerosol layer height retrieval over vegetated surfaces [6]. Use of the B band together with the γ band increases accuracy of solar-induced fluorescence from chlorophyll [7]. However, such applications require accurate reference data, including full sets of line-shape parameters, which until recently were unavailable.

The B band has been investigated in our laboratory over the years, addressing the problem of lack of accurate reference data. We determined positions, intensities and line-shape parameters of nearly 60 self-perturbed transitions from the P and R branches, see [8,9] and references therein. We concluded from these studies that the shape of self-perturbed B-band transitions can be de-

scribed with the speed-dependent Voigt profile (SDVP) [10], which accounts for effects related to the speed dependence of collisional width and shift of the line. On the other hand, line-shape effects related to the velocity-changing collisions [11,12] were not observed or were manifested as slight perturbations in the fit residuals. These effects were strongly manifested in our spectra only recently for some of the very weak, high-J transitions from the R branch, measured in the pressure range close to 1 atm [9]. In Refs. [8,9] we also presented comparison of our results with the available literature data.

In this study we present line-shape measurements of three transitions from the P branch performed with our recently upgraded spectrometer using two experimental techniques: well established cavity ring-down spectroscopy (CRDS) [13–15] and relatively new cavity mode-width spectroscopy (CMWS) [16,17]. The use of two measurement techniques enables to estimate systematic uncertainty of determined line-shape parameters and reveals possible effects related to nonlinearity of the detection system [18–20]. We observe line asymmetries, which were not detected for the P branch in our previous studies [21] apart from the P21 P21 transition [8]. With the spectra signal-to-noise ratio (SNR) up to 65000, which is 8 times higher compared to previous studies of the P branch, more line-shape effects need to be accounted for [11,12] in the pressure range as low as 1.1 kPa, as the speed-dependent Voigt profile is no longer capable to properly model the shape of transitions under investigation. We also indicate systematic differences

* Corresponding author.
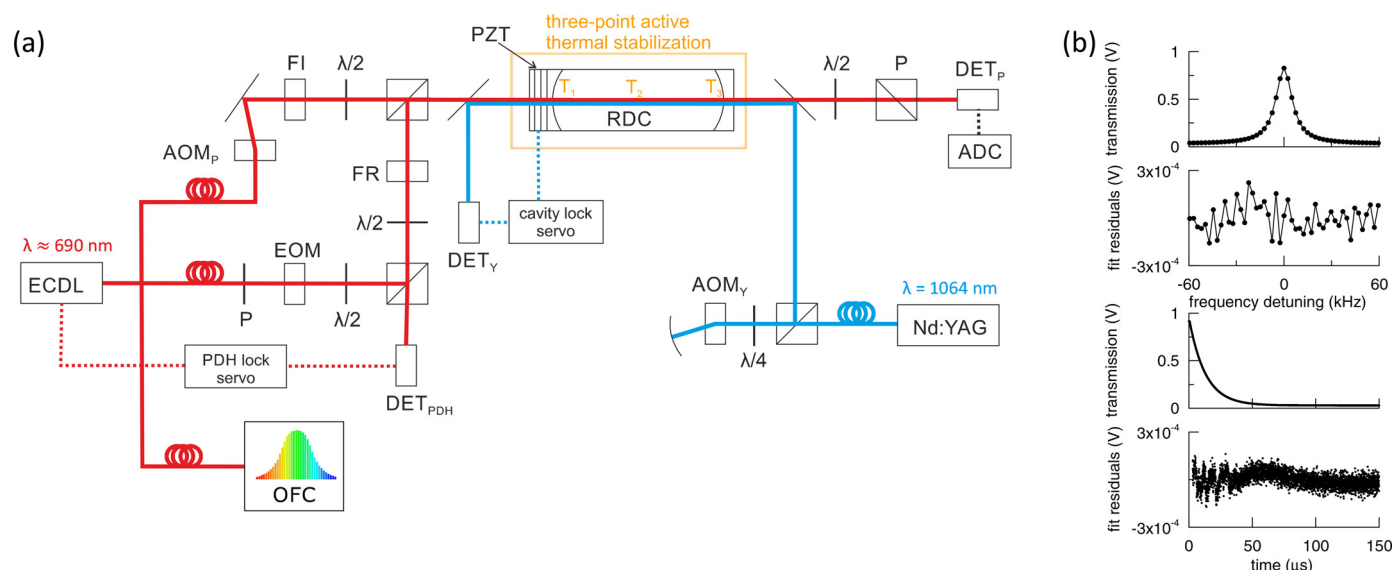*E-mail address:* kbielska@umk.pl (K. Bielska).

Fig. 1. (Color online) Panel (a): Schematic diagram of the key parts of the CRDS and CMWS spectrometer: ECDL - probe laser, Nd:YAG - iodine stabilized reference Nd:YAG laser, OFC - optical frequency comb, RDC - ring-down cavity, PZT - piezo transducer, AOM_Y , AOM_P - acousto-optic modulators, EOM - electro-optic modulator, DET_Y, DET_{PDH}, DET_P - photodetectors, FI - Faraday isolator, FR - Faraday rotator, $\lambda/2$ - half-wave plates, P - linear polarizer, ADC - analog to digital converter. Solid lines indicate laser beams, whereas dotted lines mark servo loops and electrical signals. Panel (b): In the top part the measured cavity mode together with the residuals from the fit of the Lorentzian profile whereas in the bottom part the measured ring-down decay together with the residuals from the fit of the exponential function are presented. Both of them correspond to the spectrum baseline.

of line intensities compared to previous study of the P branch performed in our laboratory [21], which may be as large as 3%.

2. Experimental setup

The experimental setup is an upgraded version of the spectrometer used in Ref. [8] (see references therein for details). The most important differences from previous version of the spectrometer are that the locking and probe beams are separated by means of polarization, the ring-down cell temperature is actively stabilized, the extinction ratio of the probe beam switching off during ring-down acquisition is improved and the source of an optical reference used for the cavity length stabilization is changed from polarization-stabilized HeNe laser to iodine-stabilized Nd:YAG laser, which has long term stability below 5 kHz.

Separating the probe beam from the locking one enables to use the spectrometer not only for the CRDS measurements, but also for CMWS. The CMWS technique relies on the change of the cavity mode shape caused by sample absorption. The high-finesse cavity TEM_{00} mode shape can be described with the Lorentzian function. Its full width at half maximum, $\delta\nu$, is increasing with increasing absorption and can be expressed through the ring-down time decay constant, τ as $\delta\nu = 1/(2\pi n \tau)$, where n is the refractive index [16]. In contrast to CRDS, the CMWS does not require high bandwidth detection system.

2.1. Experimental setup details

The spectrometer is an optical frequency comb (OFC) assisted, Pound-Drever-Hall (PDH) locked, frequency-stabilized cavity ring-down spectrometer (FS-CRDS) in dual beam configuration, which enables also measurements with the CMWS technique. Schematic diagram of the spectrometer is presented in Fig. 1 in panel (a), whereas in panel (b) there are shown the recorded ring-down signal and the cavity mode shape together with their fit residuals. The main part of the spectrometer is a 74 cm long, stainless steel ring-down cell with spherical, double-wavelength coated mirrors in non-confocal configuration, and the glass windows with anti-reflective coating. The nominal mirrors reflectivity is 99.981% in

the spectral range near 690 nm, corresponding to the oxygen B band, and 96% at 1064 nm corresponding to the Nd:YAG wavelength. The cavity free spectral range (FSR) is about 202 MHz. In the absorption-free case the ring-down time decay constant $\tau \approx 12.6$ μs, corresponding to $\delta\nu \approx 12.6$ kHz. One of the mirrors is mounted on a piezo transducer, which enables active stabilization of the cavity length, similarly as in Ref [22]. Iodine-stabilized Nd:YAG laser serves as a reference laser for the cavity length stabilization. The system enables also controlled tuning of the cavity length, which leads to the cavity modes frequencies shifting and thus enables to reduce the measurement step below the cavity FSR. The frequency step on spectra presented here is approximately 50 MHz.

The probe laser is an external cavity diode laser (ECDL) emitting in the spectral range between 687 nm and 707 nm. The laser beam is split into several beams, and the key ones are shown in Fig. 1. The first beam serves as a locking beam. It is modulated with the electro-optic modulator (EOM) driven with RF signal at 20 MHz frequency. The beam is reflected from the cavity. With the Faraday rotator and half-wave plate it is directed to the photodetector DET_{PDH}. This beam is used to lock the probe laser to the ring-down cavity with the PDH technique [23]. The laser is spectrally narrowed [24] from about 100 kHz by 3 orders of magnitude. As a result the spectral width of the laser is negligibly small comparing to the cavity mode width. The second beam has polarization orthogonal to the locking beam and serves as actual probe beam, similarly as in Ref [25]. It is detuned from the locking beam with the acousto-optic modulator (AOM_P) by one cavity FSR. Behind the cavity, the locking beam is polarizationally separated from the probe one to enable proper ring-down acquisition. An optical beatnote between the third beam and the OFC is created to determine absolute optical frequency at each point of the measured spectrum. Frequency of this beam is detuned with an AOM in double pass configuration, not shown on the scheme, to match the beatnote frequency to the bandwidth of its detection system. Other beams, not shown in Fig. 1, are used to monitor single-mode laser operation with a Fabry-Pérot interferometer and to measure optical frequency with a wavemeter, which is needed to determine the comb mode number.

The tuning range of the AOM_P, shifting the probe beam frequency (see Fig. 1), is sufficient to scan over the cavity mode. It enables determination of the mode position and the beam frequency fine tuning in order to obtain optimal transmission of the probe beam through the cavity and measure mode halfwidth for CMWS. Precise probe beam tuning to the cavity resonance together with dumping its power during the ring-down acquisition by significantly more than 58 dB (the exact value of the extinction ratio is too high to be measured) assures that the determined time decay constant required to derive sample absorption is not affected by systematic errors caused by the interference between the beam leaking from the cavity and the incompletely switched off pumping beam [26].

Separating the probe beam from the locking one enables to maintain the PDH lock during the ring-down acquisition. This significantly reduces the need for the correction of the DC offset [27], which usually accompanies PDH error signal if the system is repetitively re-locked [28–31]. Another advantage of the beams separation regards the optical power in the cavity. In the PDH locking technique, the beam is frequency modulated and thus significant part of the beam has non-resonant frequency. In our experiment this is about 30% of the locking beam power. In the present configuration of the spectrometer, the probe beam is not frequency modulated and the entire optical power is in resonance with the cavity. In this way it is possible to obtain higher optical power in the cavity at probe beam frequency than in previous configurations of our spectrometer, where the locking and probe beams were not separated, as the locking beam power is approximately 10% of the probe one.

Tuning the probe beam over the cavity mode enables determination of its width which leads to the CMWS measurement technique. However, the measurement of the cavity mode shape lasts much longer than recording ring-down decays, which limits averaging and causes that the noise on CMWS spectra is larger than on CRDS ones. As a result we use CMWS only to confirm conclusions based on CRDS measurements and to estimate systematic uncertainty of determined line-shape parameters.

All frequency counters and signal generators in the spectrometer (including AOM drivers) and the OFC are referenced to a 10 MHz RF signal [32] from a hydrogen maser [33], which serves as a link to UTC(AOS). This signal is delivered to our laboratory from the Astro-Geodynamic Observatory (AOS) in Borowiec, Poland through a fiber link [34,35] and has stability of 10^{-12} at 1 s.

The entire ring-down cavity construction is enclosed inside the thermal insulation box with active temperature stabilization. The temperature is stabilized at 296 K with the use of Peltier elements working in a cooling or heating regime as necessary. Additional small heaters are placed along the cavity to reduce the temperature gradient, equilibrating the temperature measured at three points along the cavity, i.e. in the cavity center and near the cavity mirrors. Two additional thermistors placed half-way between the cavity center and the cavity mirror are used to monitor the temperature between these points. Typical variability of the cavity temperature in time, measured in these five points during about 8 hours is shown in Fig. 2. Periodical structures visible on the plot correlate with variations of the laboratory temperature and are related to the cycle of the air conditioning system. The absolute temperature is known with uncertainty of 30 mK arising from the thermistors calibration (calibrated Fluke sensor 5641 with 1595A controller) and its uniformity defined as average standard deviation from five points equally distributed along the cavity is approximately 18 mK, thus the total standard temperature uncertainty is 35 mK.

The sample pressure is measured with calibrated baratron capacitance manometer (MKS Instruments 690A12TRA with signal conditioner 670B) of nominal accuracy at 0.05% level and full scale
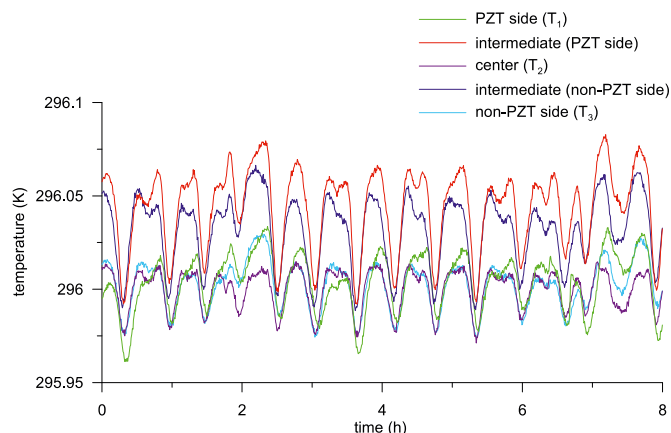

Fig. 2. (Color online) Temperature measured along the ring-down cavity vs. time: in the cavity center, T_2, at its ends, marked as PZT, T_1, and non-PZT side, T_3, and in two intermediate positions between the cavity ends and the cavity center.

pressure range of 100 Torr. Its reading is compared with a second manometer of the same type and precision, and their pressure ratio (constant within 0.07% for all measurements) is used as additional measure of the calibrated manometer stability.

2.2. Effect of laser power on cavity losses

We noticed during the tests of the new setup a significant dependence of determined value of the time decay constant, τ, and thus the absorption, on the probe beam power especially during the prior exposition of the cavity mirrors to relatively high optical power. In Fig. 3 the total cavity losses, $1/(c\tau)$, where c is the speed of light in the vacuum, are presented for the absorption-free case and for relatively high molecular absorption for different peak power levels in the cavity. In this experiment, after tuning the probe beam frequency to the resonance frequency, the probe beam was switched on for 30 s and then the time decay constant was determined 30 times. Each τ value was determined by averaging 3000 ring-down decays and the time between consecutive τ determinations in one series was approximately 3.2 s.

The top panel of Fig. 3 shows the results obtained for two different peak power levels in conditions corresponding to the spectrum baseline. An offset of nearly 0.4% in the baseline level between the results obtained for the low power case (peak power in the cavity about 80 mW) and nearly maximum available power (about 1400 mW) is observed. Panel (b) shows analogous measurement performed in conditions corresponding to about 80% of the maximum absorption which can be measured in this configuration of the experiment. Due to the absorption, the ratio between high and low power case is reduced here. The green plot, corresponding to the peak cavity power of approximately 550 mW, shows the process of the system equilibration after illuminating cavity mirrors for 30 s. This experiment shows that illuminating the spectrometer at high probe beam power may significantly perturb determined shape of transitions in the CRDS technique, as it can lead to change in the determined sum of absorption and base losses which is comparable to the offset shown in the top panel, where the ratio between high and low power is 2.5 times larger. We ascribe this effect to the changes in the cavity mirrors properties caused by their heating by the probe beam. On the other hand, similar effect is not clearly observable in our experimental setup for the CMWS technique. This may be caused by the fact that during mode shape measurement in the CMWS technique, the probe beam heats mirrors for longer time and the equilibrium point is different from the one for CRDS. As a consequence of these observations, we do not simultaneously perform measurements with
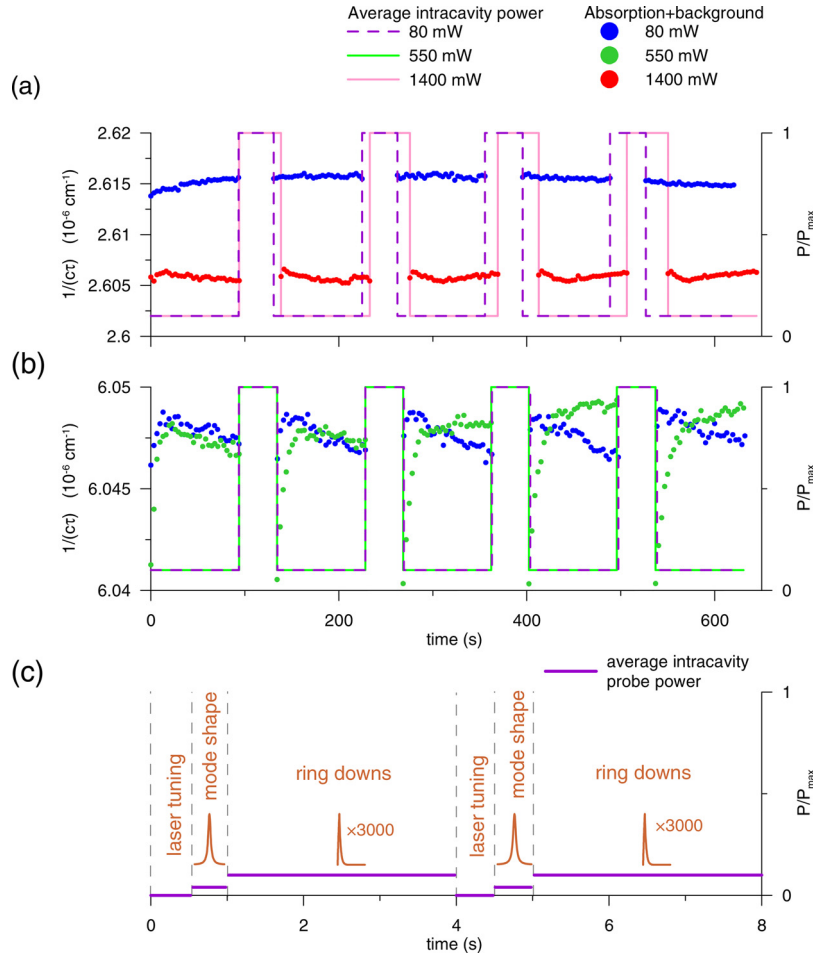
Fig. 3. (Color online) Absorption baseline (panel (a)) and the baseline plus about 80% of the maximum reliably measurable absorption (panel (b)) determined with the CRDS technique for different peak power levels in the ring-down cavity. After each series of thirty $1/(c\tau)$ determinations the procedure of finding the cavity mode was repeated and the probe beam was left on for 30 s. τ is the time decay constant whereas c is the speed of light in the vacuum. Solid and dashed lines indicate average optical power in the cavity $P/P_{\max}$ relative to the maximum power of the value indicated in the plot legend. Panel (c): typical average power waveforms during measurements with the CRDS technique, for the peak intracavity power of approximately 80 mW. Note different time scales in upper panels and panel (c). See details in the text.

these two experimental techniques, but we switch the measurement technique after collecting entire spectrum or set of spectra. Also, to obtain undistorted spectra in CRDS measurements, the peak probe beam power in the cavity is constant during measurement of the entire spectrum as the triggering ring-down decays occurs after reaching the same level of transmission through the cavity. This eliminates possibility of absorption-dependent offsets in determined absorption caused by mirrors heating. As it is shown in Fig. 3 in the panel (c), during spectra acquisition the mirrors heating power is nearly one order of magnitude lower than in panels (a) and (b) and thus the effect on the background level is negligible.

3. Data analysis and line profiles

The data analysis is performed with several line profiles. Profile which accounts for all effects observed in our spectra is a Hartmann-Tran profile (HTP) [36,37]. It is recommended by IUPAC [38] as a standard profile for spectral databases such as HITRAN [39]. Its applicability for atmospheric-related research has been confirmed for a wide range of line-shape parameters [40]. The HTP is based on a more general expression proposed by Lance et al. [41] and Pine [42] and accounts for the Doppler broadening, collisional broadening and shifting of the line as well as

their speed dependence, line narrowing due to velocity changing collisions according to the hard collision model and correlations between phase- and velocity changing collisions. Also, the line-mixing asymmetry [43] can be easily incorporated into the HTP, however we do not observe it in our spectra which were acquired in relatively low pressure conditions. In the low pressure regime the above mentioned effects can be numerically correlated and thus indistinguishable for fitting algorithms. To reduce this effect, we perform the multispectrum fitting procedure [44–46].

The speed dependence of collisional width, $B_w(x)$, and shift, $B_s(x)$, in the HTP is accounted for within the quadratic approximation. It can be expressed through the reduced width and shift functions as [47,48]:

$$B_w(x) = \frac{\gamma_L(xv_{m_A})}{\gamma_L} = 1 + a_w\left(x^2 - \frac{3}{2}\right), \tag{1}$$

$$B_s(x) = \frac{\Delta(xv_{m_A})}{\Delta} = 1 + a_s\left(x^2 - \frac{3}{2}\right). \tag{2}$$

Here x is reduced absorber velocity, i.e. ratio of the absorber velocity, v_A, over its most probable value, v_{m_A}. a_w and a_s are parameters describing the speed dependence of the thermally averaged over the Maxwellian distribution collisional width, γ_L, and collisional shift, Δ, respectively. $\gamma_L(v_A)$ and $\Delta(v_A)$ are speed-dependent collisional width and shift. To relate the above parameters to those

used in the definition of the HTP in Ref. [36], the following relations should be used: $\Gamma_0 = \gamma_L/2$, $\Gamma_2 = \Gamma_0 \cdot a_w$, $\Delta_0 = \Delta$, $\Delta_2 = \Delta_0 \cdot a_s$. Note that Γ_0 in Ref [36] is defined as half width at half maximum (HWHM), whereas in the present work γ_L is defined as full width at half maximum (FWHM).

Several simpler line profiles result from the HTP if different parameter values are constrained to zero. If correlations between phase- and velocity-changing collisions are not accounted for, i.e. correlations parameter $\eta = 0$, one obtains the speed-dependent Nelkin-Ghatak profile (SDqNGP) [41] with quadratic approximation [49]. We find the SDqNGP to be the simplest line profile capable to properly describe shapes of measured transitions in our experimental conditions.

Constraining, additionally, to zero the Dicke narrowing parameter [50], $\nu_{opt} = 0$ (frequency of the velocity-changing collisions, denoted in Ref [36] as ν_{VC}), leads to the speed-dependent Voigt profile with the quadratic approximation for the speed dependence (SDqVP) [10], which was used in most of our previous studies of the oxygen B-band transitions. No speed dependence, i.e. $a_w = 0$ and $a_s = 0$ leads to the commonly used, basic Voigt profile (VP). The Nelkin-Ghatak profile (NGP) [51] adds to the Voigt profile line narrowing due to velocity-changing collisions in hard collision model. However, it was shown in our previous studies that the NGP cannot properly reflect the shape of transitions under investigation even if the spectrum SNR is significantly lower than in the present study [21].

In addition to the above-mentioned line profiles we use the β-corrected SDqNGP and HTP [52,53]. This brings the hard-collision-based model closer to the more physically justified billiard-ball model [54–56]. The inclusion of the correction changes the value of ν_{opt} and does not affect the fit residuals and values of other parameters, in the present work. This is because in the low pressure range of our measurements the β correction is almost constant and for self-perturbed case equals to 0.691 [53]. Therefore ν_{opt} for β-corrected SDqNGP and HTP is 1.447 times bigger than those for SDqNGP and HTP, respectively.

In order to reduce numerical correlations between line-shape parameters, the multispectrum fitting procedure is performed for all the above-mentioned profiles for averaged spectra. In the fitting procedure all line-shape parameters included in the model line profile are floated apart from the Doppler broadening, constrained to value corresponding to gas temperature, wavelength and absorber molecular mass. Unperturbed transition frequency, ν_0, speed-dependent parameters, a_w and a_s, and correlations parameter, η, are fitted as constant across pressures. Other parameters, i.e. γ_L, Δ and ν_{opt}, are assumed to linearly change with concentration, N, and thus they are fitted as coefficients: γ_L/N, Δ/N and ν_{opt}/N. Additionally, line area is fitted separately for each pressure to account for potential manometer nonlinearity. During measurements the ring-down cavity temperature was stabilized at temperature $T = 296$ K and thus no temperature dependencies were accounted for in the fitting procedure.

Together with the line-shape parameters, a set of baseline parameters is fitted. This includes background, corresponding to the cavity losses in absorption-free case, and linear slope, accounting for changes in the cavity mirrors reflectivity with the wavelength. Additionally, there may occur etalons created between cavity mirrors and surfaces parallel to them [57]. In our system, the main etalon fringes are created between the reflective and AR-coated surface of the cavity mirror, having period of 26 GHz and amplitude of $2 \cdot 10^{-9}$ cm^{-1}. Other etalons occur between the cavity mirrors and cavity windows. They have period of 3 GHz or 5 GHz and typically the amplitude one order of magnitude lower from the main ones. They manifest themselves as sine-like shapes in the spectrum baseline and they are accounted for in the fitting procedure.

4. Uncertainty estimation

One of the challenges in the determination of the line-shape parameters is estimation of their systematic uncertainties. Whereas some of their contributions, such as the uncertainty in the pressure and the temperature determination, can be relatively easily accounted for, the possible influence of other factors on determined values is usually difficult to reliably evaluate. In the latter category there are factors such as the choice of particular line profile and the line shape distortion due to the apparatus function, which in the CRDS technique arises mainly from the nonlinearity of the detection system [19,20]. In our experiment additional contribution to the uncertainty arises from fitting multiple baseline parameters which may affect determined values of line-shape parameters.

Our approach to the estimation of the various contributions to the uncertainty of particular parameters is shown in details in Table 1 for the P9 P9 transition fitted with the SDqNGP. In the first row type A uncertainty, whereas in the consecutive rows contributions to type B uncertainty are given. To identify transitions we use notation $\Delta NN''\ \Delta JJ''$, with N being the rotational angular momentum quantum number and J being the total angular momentum quantum number, and the double prime indicating the lower state.

Estimation of the frequency reference accuracy contribution is based on the known relative stability of the 10 MHz reference signal ($u(f_{ref}) = 10^{-12}$ at 1 s). This relative stability is multiplied by the maximal values of line-shape parameters, corresponding to the highest measurement pressure: collisional broadening, shifting and Dicke narrowing. Its relative contribution to the transition frequency uncertainty equals $u(f_{ref})$. The instability of the source of the optical reference, i.e. Nd:YAG laser frequency instability, affects only type A uncertainty.

Uncertainty of the gas temperature measurement affects determined parameters due to its influence on the determination of the absorber concentration. In our measurements the total temperature uncertainty is about 0.035 K. At the temperature of 296 K it leads to the relative uncertainty in the absorber concentration of 0.00012 and it affects all parameters fitted as coefficients over the concentration. Additionally, the uncertainty in the temperature measurement affects the determination of temperature-dependent parameters.

The temperature dependence of the line intensity can be calculated based on the transition lower energy state, E'', and the total partition sum, $Q(T)$, both of which are available in the HITRAN database [39], according to the formula:

$$\frac{S(T)}{S(T_{ref})} = \frac{Q(T_{ref})}{Q(T)} \cdot \frac{\exp(-hcE''/k_BT)}{\exp(-hcE''/k_BT_{ref})} \cdot \frac{1 - \exp(-h\nu_0/k_BT)}{1 - \exp(-h\nu_0/k_BT_{ref})}, \quad (3)$$

where h is the Planck constant, k_B is the Boltzmann constant and $T_{ref} = 296$ K is the reference temperature. In the measurements presented here, the temperature uncertainty leads to the maximum relative line intensity uncertainty arising from its temperature dependence of 0.00007 for the P7 P7 transition.

In the HITRAN database there are given coefficients which enable estimation of the temperature dependence of the collisional broadening according to the power law [58]:

$$\frac{\gamma_L}{p}\Big|_T = \frac{\gamma_L}{p}\Big|_{T_{ref}}\left(\frac{T_{ref}}{T}\right)^n \quad (4)$$

where exponent n gives the temperature-dependence of the collisional width γ_L over pressure p. This dependency can be also expressed in terms of the concentration N as:

$$\frac{\gamma_L}{N}\Big|_T = \frac{\gamma_L}{N}\Big|_{T_{ref}}\left(\frac{T_{ref}}{T}\right)^{n-1}. \quad (5)$$

Value of $n = 0.71$ for all the oxygen B-band transitions is available in the HITRAN database [39]. This is a default value and it follows Ref [59]. Moreover, it has been determined for the air-broadened

Table 1

Contributions to the total uncertainty for parameters obtained for the P9 P9 transition fitted with the SDqNGP. Contributions to uncertainty of the unperturbed line position, ν_0, are given in kHz, whereas contributions to uncertainties of all other parameters are given as relative values. In the first row there is given type A uncertainty in CRDS measurements, i.e. fit uncertainty, whereas all other contributions are of type B. In the bottom row the total parameter uncertainty is given.

parameter	ν_0	S	γ_L/N	Δ/N	ν_{opt}/N	a_w	a_s
type A	6.7	0.00015	0.0005	0.0031	0.023	0.01	0.076
contributions to type B uncertainty:							
frequency reference accuracy	0.43	0.000013	0.000013	0.00017	0.00052	–	–
temperature measurement	–	0.00012	0.00012	0.00012	0.00012	–	–
temperature dependency	–	0.000045	0.00006	0.00006	0.00006	–	–
pressure measurement	–	0.0011	0.0011	0.0011	0.0011	–	–
choice of line profile	9.0	0.00009	–	–	–	–	–
measurement technique	24.5	0.0017	0.0066	0.012	0.59	–	0.39
baseline model uncertainty	12.2	–	0.0007	0.0051	–	–	–
total uncertainty	30.0	0.0021	0.007	0.014	0.60	0.01	0.40

lines, not for self-broadened ones. In order to not underestimate the uncertainty we decided to use lower n value of 0.5, similarly as in Ref [21]. As there is no information available on the temperature dependency of the collisional shifting and frequency of the velocity changing collisions coefficients, we assume that its relative uncertainty arising from the temperature dependency is the same as for the collisional broadening.

The pressure measurement uncertainty affects all parameters which change with the absorber concentration similarly as the temperature uncertainty. For the pressure measurement we used a baratron capacitance manometer of relative accuracy of 0.0005. Including the dependence of the pressure measurement accuracy on the measurement temperature, which was up to 2 K different from the calibration temperature, the estimated relative uncertainty in the pressure measurement is 0.0011.

In order to estimate the influence of the choice of the line profile on the determined line intensity and the unperturbed line position we compared values obtained from the SDqNGP with values obtained from the speed-dependent Nelkin-Ghatak profile with the speed-dependent functions approximated with confluent hypergeometric functions [48] (SDhNGP). These are the only parameters which can be compared in this way as all others may have different values if different line profile is used.

We performed measurements with the CMWS technique in the same pressure and temperature conditions as for CRDS. CMWS in our setup is characterized by the SNR about 60% lower than CRDS, however as it is shown in Fig. 5 it is sufficient to observe the systematic deviation of the recorded shape of transitions from the SDqVP. We compared values of the parameters obtained from measurements with these two techniques to validate systematic uncertainties. If the difference was larger than summary type A uncertainty of values obtained from CRDS and CMWS, this difference was accounted for as contribution to the uncertainty.

The possible effect of the detection system nonlinearity on the line-shape parameters has been evaluated with simulations similar to those performed in Ref [60]. The simulated ring-down decay or cavity mode shape was multiplied either by function $y_1(U) = 1 - a \cdot U/U_{max}$ or $y_2(U) = [U/U_{max}]^a$. In both functions U is the measured signal, U_{max} is its amplitude and a is the nonlinearity parameter. The effect of such signal deformation is shown in Fig. 4 as a relative error on determined line area for different values of a. For both types of nonlinearity function, errors in CRDS and CMWS techniques have opposite signs. Based on Ref [20,21], the realistic nonlinearity level may be as high as $a = 0.02$. In Table 2 there are shown simulation results for such a level of nonlinearity for both models, for CRDS and CMWS spectra. For the purpose of this comparison, a spectrum with the parameters corresponding to the P1 P1 line at the highest measured pressure of 22 Torr was simu-
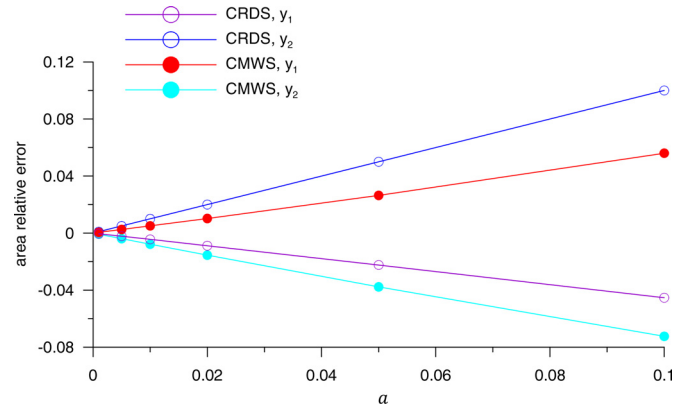

Fig. 4. (Color online) Relative error on fitted line area introduced by the nonlinearity of the light intensity conversion to measured voltage U at the level a for CRDS and CMWS spectra. The simulated nonlinearity functions are $y_1(U) = 1 - a \cdot U/U_{max}$ and $y_2(U) = [U/U_{max}]^a$ as indicated in the plot legend. U_{max} is the signal amplitude.

Table 2

Relative error introduced on particular line shape parameters and spectrum background by nonlinearity in the form of functions y_1 and y_2 for two measurement techniques.

parameter	CRDS y_1	CRDS y_2	CMWS y_1	CMWS y_2
γ_L	0.0003	-	0.000002	–0.000003
ν_{opt}	0.0003	-	–0.000007	0.00001
a_w	–0.005	-	–0.00002	0.00003
line area	–0.009	0.02	0.01	–0.015
background	–0.009	0.02	0.01	–0.015

lated. The nonlinearity of assumed types has significant effect on the line area and the background corresponding to cavity losses in the absorption-free case. In the case of the CRDS technique and nonlinearity y_1, it affects also a_w at 0.005 level, whereas the effect on other line-shape parameters is much smaller. In our experiment, the relative difference in the line intensity determined with these two measurement techniques never exceeds 0.0035, thus based on the simulations we conclude that the nonlinearity parameter also does not exceed this value.

The last contribution to systematic uncertainty is marked in Table 1 as "baseline model uncertainty". This is to account for possible different approaches to baseline parameters determination and the choice of averaged data set. To verify this we made fits with fitted or constrained parameters of the etalons. Also, fits with full set of data and about 60% best quality data were compared.
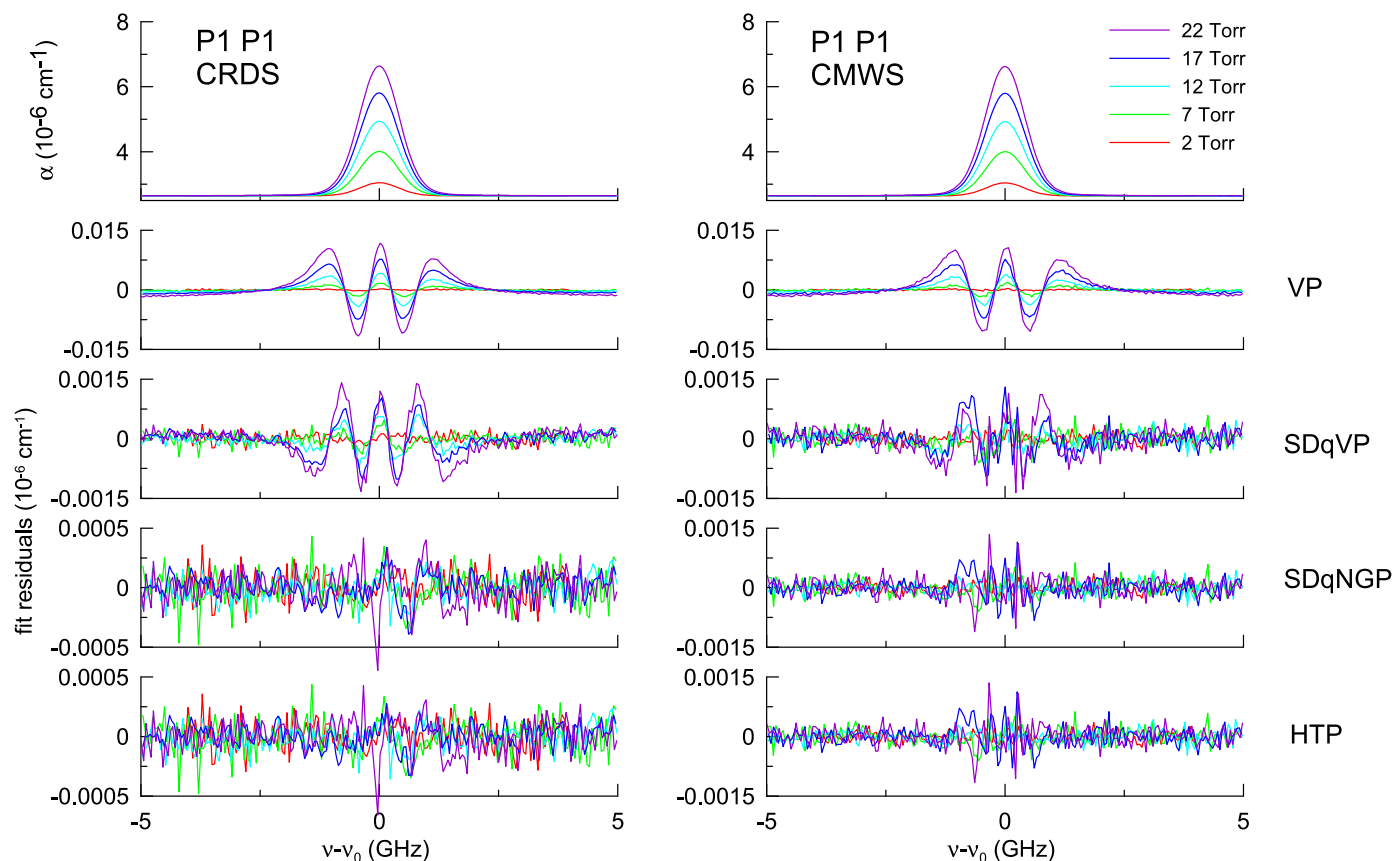
Fig. 5. (Color online) Self-perturbed P1 P1 transition measured with two experimental techniques: CRDS (left panels) and CMWS (right panels). Top panels present measured lineshape for five pressures marked with different colours. In the bottom panels there are shown fit residuals from the multispectrum fitting procedure obtained for fits with different model line profiles: VP, SDqVP, SDqNGP and HTP as marked on the right side of the plots.

5. Results and discussion

In the present study three self-perturbed transitions from the P branch of the oxygen B band are investigated, namely P1 P1, P7 P7 and P9 P9. For the measurements we used a high-purity oxygen sample (99.999%) of natural isotopic abundance. Each of the transitions was measured at five different pressures. The measurement pressure range was limited by the maximum absorption which can be measured with our spectrometer. This maximum absorption corresponds to the ring-down time decay constant $\tau \approx 4.5~\mu$s, i.e. sum of base losses and absorption, $\alpha \approx 7.4 \cdot 10^{-6}$ cm^{-1}. In order to obtain the highest spectra quality both in CRDS and CMWS, we further reduced the maximum absorption and limited the pressure range to 22 Torr, 8 Torr and 8.5 Torr for the P1 P1, P7 P7 and P9 P9 lines, respectively. To increase the spectra SNR, between 7 and 14 spectra were averaged for the CRDS technique and between 3 and 24 spectra for the CMWS at each pressure.

All transitions under investigation are fitted with the set of line profiles: VP, SDqVP, SDqNGP and HTP, with or without β-correction for the hard-collision-based profiles. Because of the low pressure range, β-correction does not introduce any changes in the residuals and so we omit plotting them and we limit ourselves only to not-corrected ones. Fit residuals from the multispectrum fitting procedure [44–46] for the P1 P1 transition are presented in Fig. 5, both for spectra obtained with CRDS and CMWS technique. Spectra recorded with CRDS as well as the corresponding fit residuals for the P7 P7 and P9 P9 transitions are shown in Fig. 6. Line-shape parameters obtained for each of the considered profiles together with their standard uncertainties are given in Table 3.

Various line-shape effects are most clearly visible for the P1 P1 line, which was measured in the widest pressure range. Also, this line is characterized by the largest collisional broadening coefficient, thus its speed dependence affects the line shape more significantly. The line-shape effects are clearly visible both in CRDS and CMWS spectra. Although the CMWS spectra are characterized by lower SNR, they confirm conclusions from CRDS measurements and enable to verify that detected line-shape effects are not artificially introduced for example by nonlinearity of the CRDS detection system.

Obviously, the commonly used VP cannot properly model the shape of considered transitions. In our previous measurements [21], performed in the lower SNR conditions, the SDqVP was able to reflect the line shape well enough. However, this profile is not sufficient to fit data in present survey. We ascribe this change to the increased SNR in our spectrometer and to the active stabilization of the ring-down cell temperature. This is especially clear for the P1 P1 transition, however also for two other lines the effect is clearly visible. In order to obtain the simplest profile which may model these lines, it is necessary to include both the speed dependence and velocity-changing collisions [63] in terms of hard collision model, i.e. use the SDqNGP [41]. The more physical approximation of the speed dependence, where reduced collisional width and shift of the line are represented with confluent hypergeometric functions, does not improve the fit quality compared to the SDqNGP. Also the HTP leads to slightly higher or identical value of the quality of the fit factor [46,64] as the SDqNGP (QF, see Table 3).

Comparison of line parameters obtained with considered profiles is shown in Fig. 8. For all parameters apart from speed-dependent parameters, a_w and a_s, values corresponding to the SDqNGP are used as the reference. Parameters are also compared with those from Ref [21] for the SDqVP. The comparison of line positions includes also values indicated as "model" which are cal-
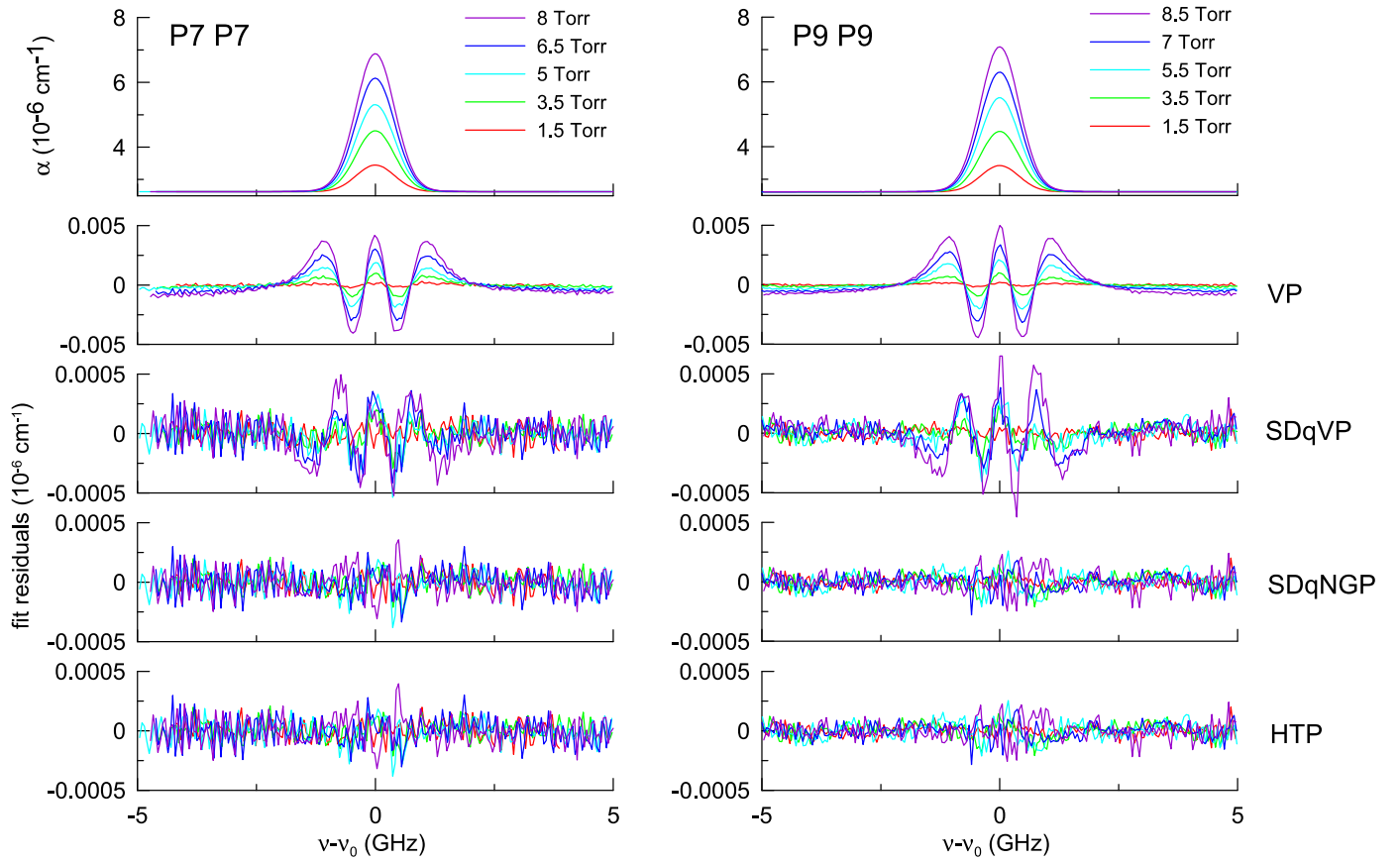
Fig. 6. (Color online) Self-perturbed transitions P7 P7 (on the left) and P9 P9 (on the right) measured at five pressures with CRDS technique. Bottom panels show fit residuals obtained in multispectrum fitting procedure performed for profiles indicated on the right.

Table 3

Line-shape parameters obtained for all considered line profiles. Uncertainties given in parentheses are total standard uncertainties determined for each line and profile. Unperturbed line position, ν_0, is given in MHz, line intensity, S, is in units $10^{-25} \mathrm{cm}^{-1}/(\mathrm{molecule/cm}^2)$, collisional broadening and shifting coefficients, as well as Dicke narrowing coefficient, γ_L/N (FWHM), Δ/N and ν_{opt}/N, are in units $10^{-19} \mathrm{GHz}/(\mathrm{molecule/cm}^3)$. To obtain values of γ_L/N, Δ/N and ν_{opt}/N in units of $\mathrm{cm}^{-1}\mathrm{atm}^{-1}$ at reference temperature $T_{\mathrm{ref}} = 296$ K values from the table should to be multiplied by 0.08270296. To compare them with the HITRAN database value of γ_L/N should be additionally divided by 2 to obtain HWHM value. Parameters in these units are given in the supplementary material. Speed-dependent parameters a_w and a_s as well as correlations parameter η are dimensionless. QF is quality-of-the-fit factor. In order to obtain a set of parameters corresponding to more physical β-corrected profiles values of ν_{opt}/N should be multiplied by 1.447, whereas other parameters remain unchanged.

line	ν_0	S	γ_L/N	Δ/N	ν_{opt}/N	a_w	a_s	η	QF
	VP								
P1 P1	435,382,026.93(26)	2.0521(35)	1.244(20)	-0.0477(43)	–	–	–	–	1684
P7 P7	434,783,508.54(11)	5.640(10)	1.024(30)	-0.0924(46)	–	–	–	–	4297
P9 P9	434,553,071.99(10)	5.565(11)	1.000(33)	-0.0932(45)	–	–	–	–	4239
	SDqVP								
P1 P1	435,382,026.910(40)	2.0629(34)	1.4342(50)	-0.0547(7)	–	0.1058(32)	0.190(15)	–	13,409
P7 P7	434,783,508.539(20)	5.652(12)	1.2167(73)	-0.0936(8)	–	0.116(19)	0.015(24)	–	33,304
P9 P9	434,553,071.992(41)	5.577(13)	1.1854(42)	-0.0943(25)	–	0.116(20)	0.015(9)	–	37,557
	SDqNGP								
P1 P1	435,382,026.908(24)	2.0620(32)	1.4141(20)	-0.0546(4)	0.046(11)	0.0666(62)	0.192(16)	–	30,838
P7 P7	434,783,508.539(20)	5.651(11)	1.2026(26)	-0.0935(7)	0.028(16)	0.0878(24)	0.015(25)	–	43,045
P9 P9	434,553,071.992(30)	5.576(12)	1.1701(80)	-0.0943(13)	0.030(18)	0.0835(9)	0.015(7)	–	65,103
	HTP								
P1 P1	435,382,026.909(24)	2.0620(32)	1.4138(73)	-0.0544(4)	0.001(9)	0.0601(71)	0.148(12)	-0.074(24)	31,838
P7 P7	434,783,508.539(20)	5.651(11)	1.2023(27)	-0.0932(7)	0.012(6)	0.0840(10)	-0.004(14)	-0.031(21)	43,223
P9 P9	434,553,071.992(40)	5.576(12)	1.1701(82)	-0.0942(26)	0.027(16)	0.0827(30)	0.0114(25)	-0.007(7)	65,103

culated based on spectroscopic constants determined in Ref [9]. The line position and collisional shifting coefficient for the P7 P7 transition are also compared to values presented in Ref [61]. They arise from fits with the speed-dependent Galatry profile [63] with hypergeometric speed-dependence (SDhGP). Total uncertainties of SDqNGP parameters are marked with solid lines.

Line positions obtained with considered profiles agree with the positions from the SDqNGP within fit uncertainties for the fitted profiles. Also, they agree with the model values and with the previous measurements from Ref [21] within their uncertainties. For the P7 P7 transition there is also available for comparison unperturbed line position and collisional shifting coefficient in Ref [61]. Our present results indicate that the unperturbed transition fre-
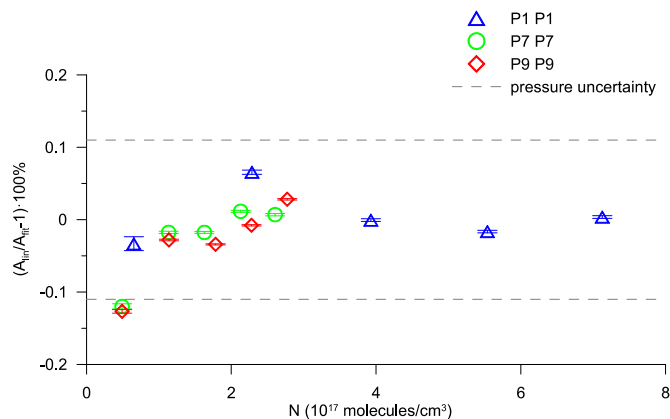
Fig. 7. (Color online) Residuals from the linear fit of line intensities to fitted values of line areas over concentration, given as relative differences. Error bars indicate the relative statistical uncertainties of the line areas. Dashed lines indicate the pressure measurement relative uncertainty.

quency is about 53 kHz higher than in Ref [61]. These values agree with each other within 3 combined standard uncertainties.

Line intensity, *S*, is retrieved from the linear dependence of the fitted line areas over concentration. In Fig. 7 fit residuals from these fits for the SDqNGP are shown for all investigated transitions. Comparison with the pressure determination uncertainty indicates expected linearity of the line areas. Comparison of line intensities is shown in panel (b) of Fig. 8. Line intensities fitted with the SDqVP and HTP agree with the reference ones from the SDqNGP. For the P7 P7 and P9 P9 transitions also values from the VP fits agree with the SDqNGP values within total measurement uncertainty, but not within the fit uncertainty. The P1 P1 line was measured in the larger pressure range, where the line-shape effects not accounted for by the VP, especially those related to the speed dependence, are more clearly visible which explains the disagreement between the line intensities obtained from fits with different profiles. Comparison to our previous values [21] indicates relative differences between 1.5% and 3%. We ascribe these differences to
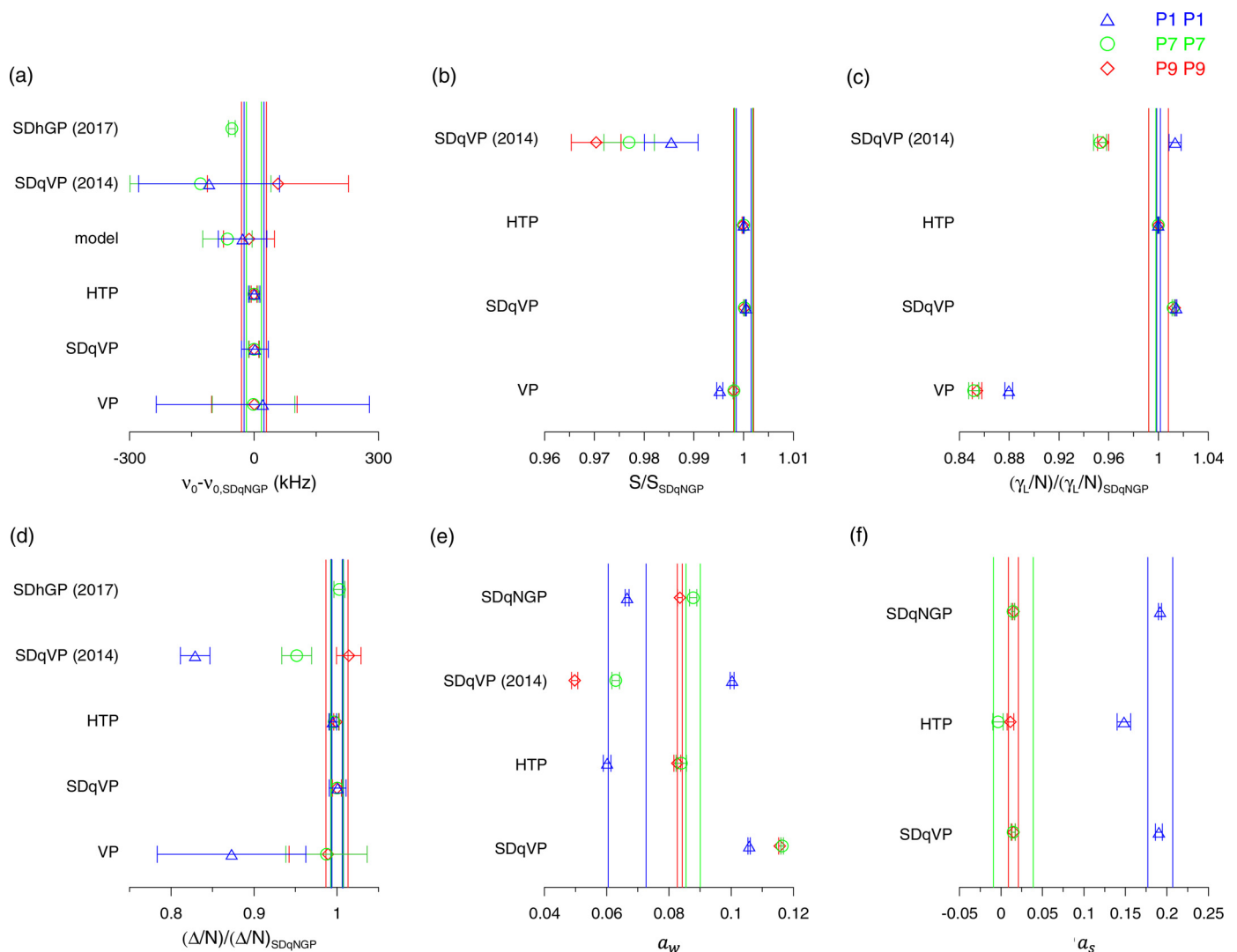

Fig. 8. (Color online) Line parameters obtained in the present work for the P1 P1 ($\triangle$), P7 P7 ($\bigcirc$) and P9 P9 ($\diamond$) transitions with different line profiles: VP, SDqVP, SDqNGP and HTP, as indicated on the left side of each panel. Comparison against the SDqNGP value for (a) line position, ν_0, (b) line intensity, *S*, (c) collisional broadening coefficient, γ_L/N, and (d) collisional shift coefficient, Δ/N, is shown. Absolute values of speed-dependence of collisional width parameter, a_w, and speed-dependence of collisional shift parameter, a_s, are plotted in panel (e) and (f), respectively. In panel (a), model indicates line positions resulting from spectroscopic constants from Ref [9]. Solid lines show the limits of total standard uncertainty for parameters resulting from the SDqNGP fit. Comparison with our previous results is marked as SDqVP (2014) [21] and SDhGP (2017) [61]. The SDqVP (2014) results are presently available in the HITRAN 2016 database [39], in the HTP parameters section, apart from the transition frequencies. The HITRAN transition frequencies, following Ref[62], vary from the values presented here by up to 1.6 MHz, however they agree within HITRAN uncertainties. Error bars indicate type A uncertainties, apart from the SDqVP (2014) and the SDhGP (2017) where error bars indicate the total standard uncertainty. (For interpretation of the references to colour in this figure legend, the reader is referred to the web version of this article.)

the lack of valid manometer calibration in our previous measurements or possible sample contamination caused by a leak in the gas delivery system.

Collisional broadening coefficient values compared to reference values from the SDqNGP fits are presented in Fig. 8 in panel (c). Differences in the values obtained with different profiles are caused by the incomplete description of the actual line shape. As it should be expected, the most significant differences occur in the VP fit, which also leads to the largest amplitude of the fit residuals. Collisional broadening coefficients from the VP fit are lower than their values from other profiles. This is caused by the fact that the VP does not account for effects leading to line narrowing, i.e. the speed dependence of the collisional width and Dicke narrowing. The SDqVP leads to collisional broadening which is between 1.2 and 1.4% larger from the reference one. The difference may be explained by the fact that it accounts with speed-dependence for Dicke narrowing. Both these effects lead to the line narrowing, however the resulting line shape is different. On the other hand, the HTP accounts for the same set of line narrowing effects as the SDqNGP and leads to collisional broadening coefficient values which agree with each other within the fit uncertainty. Comparison with the previous results [21] shows that collisional broadening coefficient previously obtained with the SDqVP agrees with the new result from the same profile for the P1 P1 transition, whereas for the other two transitions is about 4% lower form SDqNGP results and nearly 6% lower from the present SDqVP result. The difference in conclusions for different transitions may be explained by the measurement pressure range. In both, the present and the previous measurements, the pressure range was similar as it was limited by the absorption coefficient. However, the new measurements are characterized by the SNR up to 8 times higher than the data in Ref [21]. The relatively large pressure range for the P1 P1 transition enables more accurate determination of line-shape parameters even if the SNR is relatively low. On the other hand, transitions P7 P7 and P9 P9 were measured in the pressure range lower by factor of more than 2.5, which may cause that parameters were determined less accurately. Also, the absolute value of the collisional broadening coefficient is the largest for the P1 P1 transition.

Comparison of the collisional shifting coefficients, presented in Fig. 8 in panel (d), leads to conclusions significantly different from ones for collisional broadening. Here, all speed-dependent profiles apart from the SDqVP fit from Ref [21] result in coefficients values which agree with the SDqNGP ones. This is caused by the fact that all these profiles account for the line asymmetry resulting from the collisional shift's speed-dependence in the same way. In contrast to that, the VP leads to collisional shifting values which agree with the SDqNGP ones for the P7 P7 and P9 P9 transitions, whereas value for the P1 P1 line differs by nearly 13%. The difference is caused by the speed-dependent line asymmetry, which is not accounted for by the VP and it is the largest for the P1 P1 transition. Similar conclusions can be made for the previous data. In Ref [21], the speed-dependence of the collisional width was not observed, i.e. a_s was constrained to 0 which led to symmetric profile, similarly as the VP. For the P1 P1 transition, the collisional shift coefficient agrees with the value presently obtained from the VP. Pressure shift for the P7 P7 transition from Ref [21] agrees with the VP value but it is lower than our current SDqNGP reference. Previous result for the P9 P9 transition agrees with the present result. Smaller differences between VP values and previous SDqVP values for the P7 P7 and P9 P9 transitions are justified, as for these transitions absolute values of the a_s parameter is 13 times lower than for the P1 P1 line. Also, collisional shifting coefficient from Ref [61] agrees with the present result.

Values of the parameters describing speed dependence are shown in Fig. 8 in panels (e) and (f) for a_w and a_s, respectively. The a_w values fitted with the HTP agree with the SDqNGP ones
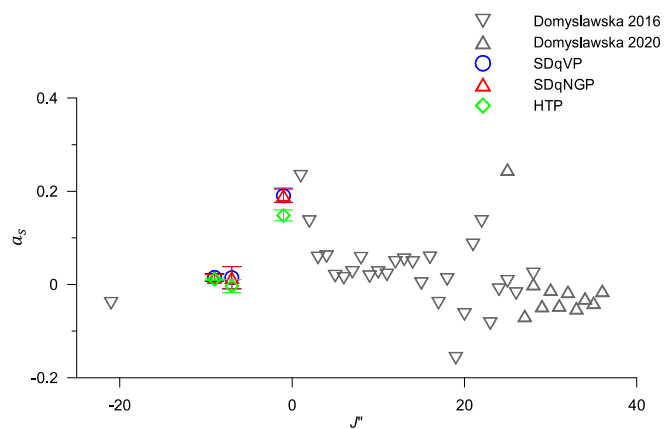

Fig. 9. Color online) Comparison of a_s values in P and R branch for investigated transitions with previous results. J'' indicates total angular momentum quantum number for the lower state and enumerates transitions. Its negative value is ascribed to P branch transitions. Grey triangles indicate a_s values by Domysławska et al. [8,9], whereas other symbols indicate present values for profiles SDqVP, SDqNGP and HTP, as indicated in the plot legend.

within the total standard uncertainty. However, if only the statistical fit uncertainty is accounted for, the a_w values from the HTP fit are slightly lower. The SDqVP leads to a_w values higher by up to 60% than the SDqNGP. This is explained by the fact that the SDqVP partially accounts with a_w for the line narrowing resulting from the velocity-changing collisions. Previous result for the SDqVP [21] nearly agrees within the total uncertainty for the P1 P1 for the same profile, similarly as in the case of the collisional broadening coefficient. For the other two transitions, previous value is lower by 46% and 57% for the P7 P7 and P9 P9 transitions, respectively. Similarly as for the collisional broadening this can be explained by the relatively low measurement pressure range and low SNR in the previous measurements.

The a_s values obtained from the SDqNGP and SDqVP agree with each other within the fit uncertainties for all considered transitions. On the other hand, for the HTP these values are lower and agree with the SDqNGP ones within the fit uncertainty only for the P9 P9 transition. This is due to the correlations parameter η, which accounts for the line asymmetry, similarly as a_s. In Fig. 9 obtained a_s values are compared with values for the R-branch transitions from Refs. [8,9]. The present results follow the pattern from the R branch: for low J'' value, a_s has relatively large value, whereas for J'' near 10 the value is close to 0.

Parameter describing frequency of the velocity-changing collisions, ν_{opt}/N, is included only in the SDqNGP and HTP among considered profiles. In the HTP fits its value is lower, especially for the P1 P1 transition where it is equal to 0 within the uncertainty, see Table 3. Due to the low measurement pressure range, it is debatable whether the determined correlations show actual value of the parameter. These values should be verified in higher SNR conditions or, preferably, wider pressure range.

6. Conclusions

We present high-SNR measurements of transitions from the O_2 B band, P branch. Due to the increased SNR compared to previously published data, we simultaneously observe the speed-dependence of the collisional broadening and the Dicke narrowing. These effects can be sufficiently well modeled with the speed-dependent hard-collision line profile or its β-corrected version. We also observe the line asymmetry caused by the speed-dependence of the collisional shift, which was not detected in previous measurements. We noticed that in our previous measurements for this

branch line intensities were systematically underestimated by up to 3% of their value. With the upgraded spectrometer, we can routinely measure the unperturbed transition frequency with uncertainty of 30 kHz, compared to 170 kHz previously. Line-shape parameters presented in this paper have been obtained from CRDS measurements and validated with the second measurement technique, CMWS, which enables us to more reliably estimate their type B uncertainties.

Author Statement

The data that support the findings of this study are available from the corresponding author upon reasonable request.

Declaration of Competing Interest

The authors declare that they have no known competing financial interests or personal relationships that could have appeared to influence the work reported in this paper.

Acknowledgments

Supplementary material

Supplementary material associated with this article can be found, in the online version, at doi:10.1016/j.jqsrt.2021.107927.

References

[1] Nowlan CR, McElroy CT, Drummond JR. Measurements of the O$_2$ A - and B- bands for determining temperature and pressure profiles from ACE-MAESTRO: forward model and retrieval algorithm. J Quant Spectrosc Radiat Transfer 2007;108(3):371–88. doi:10.1016/j.jqsrt.2007.06.006.

[2] Kuze A, Chance KV. Analysis of cloud top height and cloud coverage from satellites using the O$_2$ A and B bands a and b bands. J Geophys Res 1994;99(D7):14481. doi:10.1029/94JD01152.

[3] Yang Y, Marshak A, Mao J, Lyapustin A, Herman J. A method of retrieving cloud top height and cloud geometrical thickness with oxygen A and B bands for the Deep Space Climate Observatory (DSCOVR) mission: Radiative transfer simulations. J Quant Spectrosc Radiat Transfer 2013;122:141–9. doi:10.1016/j.jqsrt.2012.09.017.

[4] Yang Y, Meyer K, Wind G, Zhou Y, Marshak A, Platnick S, et al. Cloud products from the Earth Polychromatic Imaging Camera (EPIC): algorithms and initial evaluation. Atmos Meas Tech 2019;12(3):2019–31. doi:10.5194/amt-12-2019-2019.

[5] Yin B, Min Q, Morgan E, Yang Y, Marshak A, Davis AB. Cloud-top pressure retrieval with DSCOVR EPIC oxygen A- and B-band observations. Atmos Meas Tech 2020;13(10):5259–75. doi:10.5194/amt-13-5259-2020.

[6] Xu X, Wang J, Wang Y, Zeng J, Torres O, Reid JS, et al. Detecting layer height of smoke aerosols over vegetated land and water surfaces via oxygen absorption bands: hourly results from EPIC/DSCOVR in deep space. Atmos Meas Tech 2019;12(6):3269–88. doi:10.5194/amt-12-3269-2019.

[7] Joiner J, Yoshida Y, Guanter L, Middleton EM. New methods for the retrieval of chlorophyll red fluorescence from hyperspectral satellite instruments: simulations and application to GOME-2 and SCIAMACHY. Atmos Meas Tech 2016;9(8):3939–67. doi:10.5194/amt-9-3939-2016.

[8] Domysławska J, Wójtewicz S, Masłowski P, Cygan A, Bielska K, Trawiński RS, et al. A new approach to spectral line shapes of the weak oxygen transitions for atmospheric applications. J Quant Spectrosc Radiat Transfer 2016;169:111–21. doi:10.1016/j.jqsrt.2015.10.019.

[9] Domysławska J, Wójtewicz S, Masłowski P, Bielska K, Cygan A, Słowiński M, et al. Line-shape analysis for high J R-branch transitions of the oxygen B band. J Quant Spectrosc Radiat Transfer 2020;242:106789. doi:10.1016/j.jqsrt.2019.106789.

[10] Berman PR. Speed-dependent collisional width and shift parameters in spectral profiles. J Quant Spectrosc Radiat Transfer 1972;12(9):1331–42. doi:10.1016/0022-4073(72)90189-6.

[11] Ciuryło R, Pine A, Szudy J. A generalized speed-dependent line profile combining soft and hard partially correlated Dicke-narrowing collisions. J Quant Spectrosc Radiat Transfer 2001;68(3):257–71. doi:10.1016/S0022-4073(00)00024-8.

[12] Hartmann J-M, Boulet C, Robert D. Collisional effects on molecular spectra: laboratory experiments and models, consequences for applications. Amsterdam: Elsevier; 2008.

[13] O'Keefe A, Deacon DAG. Cavity ring-down optical spectrometer for absorption measurements using pulsed laser sources. Rev Sci Instrum 1988;59(12):2544–51. doi:10.1063/1.1139895.

[14] Long D, Cygan A, van Zee RD, Okumura M, Miller C, Lisak D, et al. Frequency-stabilized cavity ring-down spectroscopy. Chem Phys Lett 2012;536:1–8. doi:10.1016/j.cplett.2012.03.035.

[15] Maity A, Maithani S, Pradhan M. Cavity ring-down spectroscopy: recent technological advancements, techniques, and applications. Anal Chem 2021;93(1):388–416. doi:10.1021/acs.analchem.0c04329.

[16] Cygan A, Lisak D, Morzyński P, Bober M, Zawada M, Pazderski E, et al. Cavity mode-width spectroscopy with widely tunable ultra narrow laser. Opt Express 2013;21(24):29744. doi:10.1364/OE.21.029744.

[17] Long DA, Truong GW, Zee RD van, Plusquellic DF, Hodges JT. Frequency-agile, rapid scanning spectroscopy: absorption sensitivity of 2×10^{-12} cm^{-1}Hz$^{-1/2}$ with a tunable diode laser. Appl Phys B: Lasers Opt 2014;114(4):489–95. doi:10.1007/s00340-013-5548-5.

[18] Cygan A, Wcisło P, Wójtewicz S, Kowzan G, Zaborowski M, Charczun D, et al. High-accuracy and wide dynamic range frequency-based dispersion spectroscopy in an optical cavity. Opt Express 2019;27(15):21810. doi:10.1364/OE.27.021810.

[19] Wójtewicz S, Lisak D, Cygan A, Domysławska J, Trawiński RS, Ciuryło R. Line-shape study of self-broadened O$_2$ transitions measured by Pound-Drever-Hall-locked frequency-stabilized cavity ring-down spectroscopy. Physical Review A 2011;84(3):032511. doi:10.1103/PhysRevA.84.032511.

[20] Fleisher AJ, Adkins EM, Reed ZD, Yi H, Long DA, Fleurbaey HM, et al. Twenty-five-fold reduction in measurement uncertainty for a molecular line intensity. Phys Rev Lett 2019;123(4):043001. doi:10.1103/PhysRevLett.123.043001.

[21] Wójtewicz S, Cygan A, Masłowski P, Domysławska J, Lisak D, Trawiński R, et al. Spectral line shapes of self-broadened P-branch transitions of oxygen B band. J Quant Spectrosc Radiat Transfer 2014;144:36–48. doi:10.1016/j.jqsrt.2014.03.029.

[22] Hodges JT, Layer HP, Miller WW, Scace GE. Frequency-stabilized single-mode cavity ring-down apparatus for high-resolution absorption spectroscopy. Rev Sci Instrum 2004;75(4):849–63. doi:10.1063/1.1666984.

[23] Drever RWP, Hall JL, Kowalski FV, Hough J, Ford GM, Munley AJ, et al. Laser phase and frequency stabilization using an optical resonator. Appl Phys B 1983;31(2):97–105. doi:10.1007/BF00702605.

[24] Salomon C, Hils D, Hall JL. Laser stabilization at the millihertz level. Journal of the Optical Society of America B 1988;5(8):1576. doi:10.1364/JOSAB.5.001576.

[25] Cygan A, Wcisło P, Wójtewicz S, Masłowski P, Hodges JT, Ciuryło R, et al. One-dimensional frequency-based spectroscopy. Opt Express 2015;23(11):14472. doi:10.1364/OE.23.014472.

[26] Wójtewicz S, Cygan A, Domysławska J, Bielska K, Morzyński P, Masłowski P, et al. Response of an optical cavity to phase-controlled incomplete power switching of nearly resonant incident light. Opt Express 2018;26(5):5644. doi:10.1364/OE.26.005644.

[27] Cygan A, Lisak D, Wójtewicz S, Domysławska J, Trawiński RS, Ciuryło R. Active control of the Pound-Drever-Hall error signal offset in high-repetition-rate cavity ring-down spectroscopy. Meas Sci Technol 2011;22(11). doi:10.1088/0957-0233/22/11/115303.

[28] Fox RW, Oates CW, Hollberg LW. Stabilizing diode lasers to high-finesse cavities. Cavity-enhanced spectroscopies. van Zee RD, Looney JP, editors. New York: Academic Publisher Location; 2002.

[29] van Leeuwen NJ, Diettrich JC, Wilson AC. Periodically locked continuous-wave cavity ringdown spectroscopy. Appl Opt 2003;42(18):3670. doi:10.1364/AO.42.003670.

[30] Martínez RZ, Metsälä M, Vaittinen O, Lantta T, Halonen L. Laser-locked, high-repetition-rate cavity ringdown spectrometer. Journal of the Optical Society of America B 2006;23(4):727. doi:10.1364/JOSAB.23.000727.

[31] Cygan A, Lisak D, Masłowski P, Bielska K, Wójtewicz S, Domysławska J, et al. Pound-Drever-Hall-locked, frequency-stabilized cavity ring-down spectrometer. Rev Sci Instrum 2011;82(6):063107. doi:10.1063/1.3595680.

[32] Cygan A, Wójtewicz S, Kowzan G, Zaborowski M, Wcisło P, Nawrocki J, et al. Absolute molecular transition frequencies measured by three cavity-enhanced spectroscopy techniques. J Chem Phys 2016;144(21):214202. doi:10.1063/1.4952651.

[33] Jiang Z, Czubla A, Nawrocki J, Lewandowski W, Arias EF. Comparing a GPS time link calibration with an optical fibre self-calibration with 200 ps accuracy. Metrologia 2015;52(2):384–91. doi:10.1088/0026-1394/52/2/384.

[34] Morzyński P, Bober M, Bartoszek-Bober D, Nawrocki J, Krehlik P, Śliwczyński L, Lipiński M, Masłowski P, Cygan A, Dunst P, Garus M, Lisak D, Zachorowski J, Gawlik W, Radzewicz C, Ciuryło R, Zawada M. Absolute measurement of the $^1S_0 - ^3P_0$ clock transition in neutral ^{88}Sr over the 330 km-long stabilized fibre optic link. Sci Rep 2015;5(1):17495. doi:10.1038/srep17495.

[35] Krehlik P, Śliwczyński Ł, Buczek L, Kołodziej J, Lipiński M. Ultrastable long-distance fibre-optic time transfer: active compensation over a wide range of delays. Metrologia 2015;52(1):82–8. doi:10.1088/0026-1394/52/1/82.

[36] Ngo N, Lisak D, Tran H, Hartmann JM. An isolated line-shape model to go beyond the Voigt profile in spectroscopic databases and radiative transfer codes. J Quant Spectrosc Radiat Transfer 2013;129:89–100. doi:10.1016/j.jqsrt.2013.05.034.

[37] Ngo N, Lisak D, Tran H, Hartmann JM. Erratum to "An isolated line-shape model to go beyond the Voigt profile in spectroscopic databases and radiative transfer codes" [J. Quant. Spectrosc. Radiat. Transf. 129 (2013) 89100]. J Quant Spectrosc Radiat Transfer 2014;134:105. doi:10.1016/j.jqsrt.2013.10.016.

[38] Tennyson J, Bernath PF, Campargue A, Császár AG, Daumont L, Gamache RR, et al. Recommended isolated-line profile for representing high-resolution spectroscopic transitions (IUPAC Technical Report). Pure Appl Chem 2014;86(12):1931–43. doi:10.1515/pac-2014-0208.

[39] Gordon IE, Rothman LS, Hill C, Kochanov RV, Tan Y, Bernath PF, et al. The HITRAN2016 molecular spectroscopic database. J Quant Spectrosc Radiat Transfer 2017;203:3–69. doi:10.1016/j.jqsrt.2017.06.038.

[40] Ngo N, Lin H, Hodges J, Tran H. Spectral shapes of rovibrational lines of CO broadened by He, Ar, Kr, Hartmann, and SF_6: a test case of the hartmann-Tran profile. J Quant Spectrosc Radiat Transfer 2017;203:325–33. doi:10.1016/j.jqsrt.2017.03.001.

[41] Lance B, Blanquet G, Walrand J, Bouanich JP. On the speed-dependent hard collision lineshape models: application to C_2H_2 perturbed by Xe. J Mol Spectrosc 1997;185(2):262–71. doi:10.1006/jmsp.1997.7385.

[42] Pine A. Asymmetries and correlations in speed-dependent Dicke-narrowed line shapes of argon-broadened HF. J Quant Spectrosc Radiat Transfer 1999;62(4):397–423. doi:10.1016/S0022-4073(98)00112-5.

[43] Ciuryło R, Pine A. Speed-dependent line mixing profiles. J Quant Spectrosc Radiat Transfer 2000;67(5):375–93. doi:10.1016/S0022-4073(00)00030-3.

[44] Benner DC, Rinsland CP, Devi VM, Smith MAH, Atkins D. A multispectrum nonlinear least squares fitting technique. J Quant Spectrosc Radiat Transfer 1995;53(6):705–21. doi:10.1016/0022-4073(95)00015-D.

[45] Pine A, Ciurylo R. Multispectrum fits of Ar-broadened HF with a generalized asymmetric lineshape: effects of correlation, hardness, speed dependence, and collision duration. J Mol Spectrosc 2001;208(2):180–7. doi:10.1006/jmsp.2001.8375.

[46] Bui TQ, Long DA, Cygan A, Sironneau VT, Hogan DW, Rupasinghe PM, Ciuryło R, Lisak D, Okumura M. Observations of Dicke narrowing and speed dependence in air-broadened CO_2 lineshapes near 2.06 μm. J Chem Phys 2014;141(17). doi:10.1063/1.4900502.

[47] Priem D, Rohart F, Colmont JM, Wlodarczak G, Bouanich JP. Lineshape study of the $J = 3 \leftarrow 2$ rotational transition of CO perturbed by N_2 and O_2. J Mol Struct 2000;517–518:435–54. doi:10.1016/S0022-2860(99)00268-9.

[48] Ward J, Cooper J, Smith EW. Correlation effects in the theory of combined Doppler and pressure broadening - I. Classical theory. J Quant Spectrosc Radiat Transfer 1974;14(7):555–90. doi:10.1016/0022-4073(74)90036-3.

[49] Rohart F, Mader H, Nicolaisen HW. Speed dependence of rotational relaxation induced by foreign gas collisions: studies on CH_3F by millimeter wave coherent transients. J Chem Phys 1994;101:6475–86. doi:10.1063/1.468342.

[50] Dicke RH. The effect of collisions upon the Doppler width of spectral lines. Physical Review 1953;89(2):472–3. doi:10.1103/PhysRev.89.472.

[51] Nelkin M, Ghatak A. Simple binary collision model for van Hove's $G_s(r, t)$. Physical Review 1964;135(1A):A4–9. doi:10.1103/PhysRev.135.A4.

[52] Wcisło P, Gordon I, Tran H, Tan Y, Hu S-M, Campargue A, Kassi S, Romanini D, Hill C, Kochanov R, Rothman L. The implementation of non-Voigt line profiles in the HITRAN database: H_2 case study. J Quant Spectrosc Radiat Transfer 2016;177:75–91. doi:10.1016/j.jqsrt.2016.01.024.

[53] Konefał M, Słowiński M, Zaborowski M, Ciuryło R, Lisak D, Wcisło P. Analytical-function correction to the Hartmann-Tran profile for more reliable representation of the Dicke-narrowed molecular spectra. J Quant Spectrosc Radiat Transfer 2020;242:106784. doi:10.1016/j.jqsrt.2019.106784.

[54] Blackmore R. A modified Boltzmann kinetic equation for line shape functions. J Chem Phys 1987;87(2):791–800. doi:10.1063/1.453286.

[55] Lindenfeld MJ. Self-structure factor of hard-sphere gases for arbitrary ratio of bath to test particle masses. J Chem Phys 1980;73(11):5817–29. doi:10.1063/1.440066.

[56] Ciuryło R, Shapiro DA, Drummond JR, May AD. Solving the line-shape problem with speed-dependent broadening and shifting and with Dicke narrowing. II. Application. Physical Review A 2001;65(1):012502. doi:10.1103/PhysRevA.65.012502.

[57] Fox RW, Hollberg L. Role of spurious reflections in ring-down spectroscopy. Opt Lett 2002;27(20):1833. doi:10.1364/OL.27.001833.

[58] Rothman L, Gordon I, Barbe A, Benner D, Bernath P, Birk M, et al. The HITRAN 2008 molecular spectroscopic database. J Quant Spectrosc Radiat Transfer 2009;110(9–10):533–72. doi:10.1016/j.jqsrt.2009.02.013.

[59] Gordon IE, Rothman LS, Toon GC. Revision of spectral parameters for the B- and γ-bands of oxygen and their validation against atmospheric spectra. J Quant Spectrosc Radiat Transfer 2011;112(14):2310–22. doi:10.1016/j.jqsrt.2011.05.007.

[60] Cygan A, Fleisher AJ, Ciuryło R, Gillis KA, Hodges JT, Lisak D. Cavity buildup dispersion spectroscopy. Communications Physics 2021;4(1):14. doi:10.1038/s42005-021-00517-3.

[61] Bielska K, Wójtewicz S, Morzyński P, Ablewski P, Cygan A, Bober M, et al. Absolute frequency determination of molecular transition in the Doppler regime at kHz level of accuracy. J Quant Spectrosc Radiat Transfer 2017;201:156–60. doi:10.1016/j.jqsrt.2017.07.010.

[62] Yu S, Drouin BJ, Miller CE. High resolution spectral analysis of oxygen. IV. energy levels, partition sums, band constants, RKR potentials, Energy Franck-Condon factors involving the $X^3\Sigma_g^-$, $a^1\Delta_g$ and $b^1\Sigma_g^+$ states. J Chem Phys 2014;141(17):174302. doi:10.1063/1.4900510.

[63] Ciurylo R, Szudy J. Speed-dependent pressure broadening and shift in the soft collision approximation. J Quant Spectrosc Radiat Transfer 1997;57(3):411–23. doi:10.1016/S0022-4073(96)00078-7.

[64] Cygan A, Lisak D, Wójtewicz S, Domysławska J, Hodges JT, Trawiński RS, Ciuryło R. High-signal-to-noise-ratio laser technique for accurate measurements of spectral line parameters. Physical Review A 2012;85(2):022508. doi:10.1103/PhysRevA.85.022508.